JOURNAL OF GEOPHYSICAL RESEARCH, VOL. 114, F02006, doi:10.1029/2008JF001025, 2009

On the effects of divide migration, along-ridge flow, and basal sliding on isochrones near an ice divide

Carlos Martín,[1] Richard C. A. Hindmarsh,[1] and Francisco J. Navarro[2]

Received 25 March 2008; revised 19 January 2009; accepted 30 January 2009; published 14 April 2009.

[1] Radar layer geometry in divide areas is strongly influenced by the operation of the Raymond effect, which causes upwarping of the layers as a consequence of the nonlinear rheology of ice. The detailed geometry of these layers is known to store a record of change in the cryosphere, of local thinning, and of the age of formation of the divide and has been surmised to provide information about lateral motion of divides. Such lateral motion can be caused by changes in flanking ice streams, and the divide area thereby contains a record of ice stream dynamics. It has also been suggested that a large perturbation of divide position will obliterate the cumulative effects of the operation of the Raymond mechanism, leading to the disappearance of Raymond bumps. Since the Raymond effect has a strong influence on the age-depth relation in ice cores, knowledge of whether its operation is localized (leading to strong bump formation) or distributed is crucial in the interpretation of ice cores. The detailed evolution of ice divide radar layer geometry remains poorly understood. Employing a full thermomechanically coupled transient model, we qualitatively explore the effect of divide migration on radar layer geometry. Certain qualitative features emerge which can be used to infer history of cryosphere change, in particular, in areas distant from the usual sites of geological dating. There remains uncertainty about the influence of sliding on the operation of the Raymond effect. Under certain conditions, the existence of sliding can damp or eliminate the operation of the Raymond effect. If this is generally true, then dating of ice divides may simply be a date for the freezing of the divide bottom. We show that sliding does not necessarily eliminate the formation of bumps. Dates of divide formation are likely to be dates for the location of the ridge at a particular spot. Raymond bump evolution is weakened by flow along the ridge. We explore quantitatively the strength of this effect, using a scaling analysis to show that the weakening can efficiently be described by one parameter, the ratio of along-ridge slope to a measure of the across-divide curvature.

Citation: Martín, C., R. C. A. Hindmarsh, and F. J. Navarro (2009), On the effects of divide migration, along-ridge flow, and basal sliding on isochrones near an ice divide, *J. Geophys. Res.*, *114*, F02006, doi:10.1029/2008JF001025.

1. Introduction

[2] Radio echo sounding of ice commonly reveals reflecting internal layers that are assumed to be isochrones. Beneath ice divides the radar layers frequently exhibit anticlines (arches known as Raymond bumps), which are a consequence of the nonlinear rheology of ice. This phenomenon was first predicted by *Raymond* [1983] and is known as the Raymond effect.

[3] Raymond bump evolution is strongly related to ice thickness history and thinning rate, and is often the only way of estimating these [*Conway et al.*, 1999]. In particular, the time at which a flow divide formed at a particular place can be estimated from the amplitude of the Raymond bumps. Consequently, a detailed physical understanding of the Raymond effect has ramifications for ice sheet history. In this paper we investigate, using a full Stokes thermomechanically coupled transient model, the effects of ice divide motion, along-ridge flow and basal sliding on the geometry of the Raymond bumps.

[4] The geometry of these arches depends upon the accumulation rate [*Nereson and Raymond*, 2000; *Nereson and Waddington*, 2002], the evolving geometry of the ice mass [*Hindmarsh*, 1996; *Nereson et al.*, 1998a, 1998b; *Nereson and Raymond*, 2001; *Nereson and Waddington*, 2002], the rheology of the ice [*Pettit and Waddington*, 2003; *Martín et al.*, 2006; *Pettit et al.*, 2007], the surface temperature and the geothermal heat flux [*Hvidberg*, 1996; *Nereson and Waddington*, 2002], the basal sliding [*Pettit et al.*, 2003], and the onset of divide flow [*Conway et al.*, 1999; *Martín et al.*, 2006], all of which are rather poorly constrained. The combined effect of some of these processes is to diminish bump amplitude; for example divide migration [*Nereson and Waddington*, 2002], stochastic

[1] British Antarctic Survey, Cambridge, UK.
[2] Departamento de Matemática Aplicada, Universidad Politécnica de Madrid, Madrid, Spain.

0148-0227/09/2008JF001025$09.00

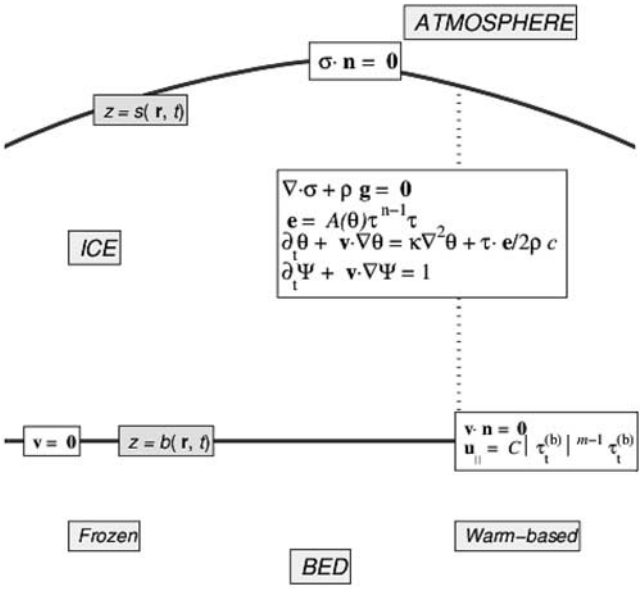

Figure 1. Illustration of the problem setup and notation.

variations of divide position [*Hindmarsh*, 1996], strong basal sliding [*Pettit et al.*, 2003] or near-linear rheologies at low deviatoric stresses [*Pettit and Waddington*, 2003]. A vertically orientated crystal fabric is predicted to increase the size of the isochrone arch [*Pettit et al.*, 2007].

[5] The ice surface is extremely flat in the along-ridge direction perpendicular to the divide flow plane, even by comparison with the divide, and the along-ridge flow and stresses are usually neglected [e.g., *Raymond*, 1983; *Hvidberg*, 1996]. Given all the factors described above, the quantification of the effects of slight transverse flow in the ice divide region is crucial to understand layer geometry and to interpret the age-depth relation from ice cores. We use an approximate 3-D model of an ice divide which exploits the smallness of the along-ridge flow to analyze this effect and we show that the along-ridge flow has to be substantial in order to reduce the Raymond effect significantly.

[6] In many places in Antarctica during the glacial period, ice was much thicker, which normally leads to warming at the base of the ice through the greater insulating effect. *Pettit et al.* [2003] have shown that when a linear relation in the basal sliding law is considered, the Raymond effect is sharply reduced. The implication of this is that the onset of operation of the Raymond effect may date the time of freezing of the base of the ice rather than some other flow change. Independently of whether the basal velocity is the result of sliding over the bedrock, deformation of basal sediments or both, the relation between basal velocity and basal stress is unclear. Different studies have assumed the basal sliding relation as slightly nonlinear [*Boulton and Hindmarsh*, 1987], highly nonlinear [*Kamb*, 1991; *Hooke et al.*, 1997] or Coulomb plastic [*Tulaczyk et al.*, 2000]. In this paper we assume a nonlinear Weertman-type sliding law [*Weertman*, 1957] and we show that as the nonlinearity is increased the damping effect of sliding upon bump amplitude is reduced and, in some cases, can increase the amplitude.

[7] We also study how the rate of ice divide migration affects the shape of the Raymond bumps stack. *Jacobson and Waddington* [2005] proposed that following a rapid divide migration relic Raymond bumps are left in a flank position where they are carried away with the flow while *Nereson et al.* [1998b] and *Nereson and Waddington* [2002] concluded that the tilt in the Raymond arch apex beneath Siple Dome (WAIS) is an indicator of a slow divide migration. In this paper, we use a transient numerical model to study the evolution of isochrones under different divide migration scenarios. We show how a slow migration, in response of progressive changes in the ice flux at the flanks, produces a tilt in the apices of the arches (e.g., Siple Dome, WAIS) while rapid migrations, as responses to instantaneous variations at the flanks, leave relict Raymond bumps in a flanking position where they are advected with the flow, while new ones are developed at the new stationary position (e.g., at Roosevelt Island, Antarctica).

[8] Finally, we show the necessity of considering the full Stokes equations to study the ice divide area. The shallow ice approximation [e.g., *Hutter*, 1983] is unable to reproduce the Raymond effect. However, there are some approximations to the momentum balance equations that can replicate the Raymond effect, particularly those considering horizontal gradients of longitudinal stresses (LMLa models [*Hindmarsh*, 2004]), usually known as high order or first-order models [e.g., *Blatter*, 1995; *Saito et al.*, 2003; *Pattyn*, 2003]. In this paper, we quantitatively compare the Raymond effect produced by the latter models with our full Stokes model.

2. Governing Equations and Numerical Model

2.1. Basic Equations

[9] The flow setup is illustrated in Figure 1 and a list of symbols is given in the notation section. The coordinates are (x, y, z), where x is taken in the direction of divide flow, y in the direction of divide ridge and z direction is the vertical. Denoting $\mathbf{r} = (x, y)$, the thickness of the ice is given by $z = H(\mathbf{r}, t)$, while the ice surface and bed and the bottom of the rock layer considered are given by $z = s(\mathbf{r}, t)$, $z = b(\mathbf{r}, t)$, $z = b_r(\mathbf{r}, t)$ respectively, and t represents time. Superscripts (s), (b) and (b_r) indicate evaluation at the surface, base and the bottom of the rock layer. The operators ∇_H, $\nabla_H\cdot$, represent the horizontal gradient and divergence respectively.

[10] The three-dimensional velocity field is represented by the vertical velocity w and the horizontal velocity vector $\mathbf{u} = (u_x, u_y)$, and we also use $\mathbf{v} = (u_x, u_y, w)$. The volume flux $\boldsymbol{Q} = \int_b^s \boldsymbol{u}\mathrm{d}z$ is used frequently throughout the paper. The temperature and the age are represented by θ and Ψ respectively.

[11] The mechanical equations are

$$\nabla_H\cdot\mathbf{u} + \partial_z w = 0, \qquad b(\mathbf{r},t) < z < s(\mathbf{r},t), \tag{1}$$

$$\nabla\cdot\boldsymbol{\sigma} + \rho\mathbf{g} = \mathbf{0}, \qquad b(\mathbf{r},t) < z < s(\mathbf{r},t), \tag{2}$$

and

$$\boldsymbol{\sigma}^{(s)}\cdot\mathbf{n}^{(s)} = \mathbf{0}, \quad z = s(\mathbf{r}, t), \tag{3}$$

$$\mathbf{v}^{(b)} = \begin{cases} C \parallel \boldsymbol{\tau}_t^{(b)} \parallel^{m-1} \boldsymbol{\tau}_t^{(b)} & \theta^{(b)} > \theta^f \\ \mathbf{0} & \text{otherwise} \end{cases}, \quad z = b(\mathbf{r}, t). \tag{4}$$

[12] Equation (1) expresses conservation of mass in the ice and (2)–(4) describe conservation of momentum in the ice. $\boldsymbol{\sigma}$ is the stress tensor, ρ is the density of ice, $\mathbf{g} = g(0, 0, -1)$ is the gravitational acceleration vector, $\mathbf{n}$ is the normal vector. Equation (4) is a nonlinear Weertman sliding relation with index m, where θ^f represents the melting point temperature, and $\boldsymbol{\tau}_t^{(b)}$ represents the tangential traction and C the slipperiness at the ice-bedrock interface.

[13] The kinematic equation at the surface is

$$\partial_t s + \mathbf{u}\cdot\nabla s = w + a, \quad z = s(\mathbf{r}, t), \tag{5}$$

where a is accumulation rate of ice, expressed as a volume rate per unit area.

[14] The heat equations are

$$\partial_t\theta + \mathbf{v}\cdot\nabla\theta = \kappa\nabla^2\theta + \frac{1}{\rho c}D, \qquad b_r(\mathbf{r}, t) < z < s(\mathbf{r}, t), \tag{6}$$

$$\theta^{(s)} - \theta^s = 0, \qquad z = s(\mathbf{r}, t), \tag{7}$$

$$-K_r\nabla\theta^{(b_r)}\cdot\mathbf{n}^{(b_r)} = Q_G, \quad z = b_r(\mathbf{r}, t), \tag{8}$$

where θ^s is the prescribed surface temperature, κ is the thermal diffusivity of ice, c is the specific heat capacity, $D = (1/2)$ trace $(\boldsymbol{\tau}\cdot\boldsymbol{e})$ is the dissipation, $\boldsymbol{\tau}$ is the deviatoric stress, $\tau^2 = (1/2)$ trace $(\boldsymbol{\tau}^2)$ is the deviatoric stress invariant, $\mathbf{e}$ is the strain rate, K is the thermal conductivity, and Q_G is the geothermal heat flux. We assume a nondeformable bedrock, so that in the region $b_r(r, t) < z < b(r, t)$ the velocity is zero and the advective term vanishes.

[15] The evolution equation for the age is

$$\partial_t\Psi + \mathbf{u}\cdot\nabla_{\mathrm{H}}\Psi + w\partial_z\Psi = 1, \quad b(\mathbf{r}, t) < z < s(\mathbf{r}, t), \tag{9}$$

$$\Psi^{(s)} = 0, \qquad z = s(\mathbf{r}, t), \tag{10}$$

where equation (10) expresses that the age at surface is zero, as the modelled area is located in the accumulation zone of the ice sheet.

[16] The Glen power law rheology [*Glen*, 1955] is used to describe the flow of ice,

$$e = A(\theta)\tau^{n-1}\boldsymbol{\tau} \tag{11}$$

or

$$\boldsymbol{\tau} = 2B(\theta)\, e^{(1/n)-1}\mathbf{e} \tag{12}$$

where $A = (2B)^{-n}$.

[17] We use the *Dahl-Jensen* [1989] relationship for the softness parameter $A(\theta)$,

$$A(\theta) = \{0.2071\exp(0.5978\,\theta_c) + 0.09833\exp(0.14747\,\theta_c)\} \times 10^{-15}\,\mathrm{Pa}^{-3}\,\mathrm{a}^{-1} \tag{13}$$

with $n = 3$ and $\theta_c = \theta - 273.16$ (i.e., is given in °C).

[18] In the isothermal experiments (section 3) the temperature was set throughout the column of ice to be −20°C, implying $A = 5 \times 10^{-18}$ Pa^{-3} a^{-1}. In the thermomechanical experiments (section 4), we set the upper surface temperature θ^s to −30°C and the geothermal heat flux $Q_G = 60$ mW m^{-2}. For ice and rock, the thermal conductivity is $K = 2.10$ W m^{-1} K^{-1} and the specific heat capacity is $c = 2009.0$ J kg^{-1} K^{-1} (the values of thermal conductivity and diffusivity for ice fall within the typical range for sedimentary rocks [e.g., *Pettit et al.*, 2003]).

[19] We will consider plane flow in the (x, z) plane throughout the paper except in section 3.1 where we will discuss the influence of along-ridge flow (y direction), using an approximation described below to decouple the y momentum balance from the (x, z) momentum balance. We solve the above dynamic and thermal equations using finite element methods, while semi-Lagrangian methods are used to solve the free surface evolution and age equations. The numerical model is an improved version of that described by *Martín et al.* [2006]; details of the improvements (transient temperature evolution and basal sliding) are given in the Appendix B.

2.2. Boundary Conditions at the Flanks

[20] Natural or physically intuitive boundary conditions corresponding to real ice sheet margins are so spatially remote that the computational domain required would be unfeasibly large. A sensible choice for boundary conditions for the Stokes system at the sides, which has been adopted by, for example, *Raymond* [1983], *Waddington et al.* [2005], *Hvidberg* [1996], and *Martín et al.* [2006], is to impose shallow ice velocity fields, which export ice at a rate that conserves global mass. Zero horizontal heat flux at the flanks is assumed as a boundary condition for the heat equation.

[21] The velocity and temperature boundary conditions at the flanks are not exact solutions of the governing equations. The error induced on the solution propagates into the solution domain by a few times the ice thickness. To avoid this problem, following *Hvidberg* [1996], we use a solution domain extending 15 times the divide thickness at each flank but restrict our analysis of the Raymond effect to a region extending only 5 times the divide thickness at each flank.

2.3. Scale Analysis

[22] A scale analysis presented in Appendix A shows that the slope of the ice surface at a distance of the order of one ice sheet thickness away from the divide, γ_x, is given by

$$\gamma_x \equiv \partial_x s(x = H) \sim \Lambda \equiv \frac{2B}{\rho_i g H^*}\left(\frac{a^*}{H^*}\right)^{\frac{1}{n}} \ll 1, \tag{14}$$

Table 1. Scale Estimates of 1000 Λ for Different Glaciological Parameters[a]

	$\theta = 0$°C			$\theta = -10$°C			$\theta = -30$°C			$\theta = -55$°C	
H (km)	$a = 0.03$	$a = 0.1$	$a = 0.3$	$a = 0.03$	$a = 0.1$	$a = 0.3$	$a = 0.03$	$a = 0.1$	$a = 0.3$	$a = 0.03$	$a = 0.1$
3	*0.17*	*0.26*	0.55	0.37	0.55	1.2	**0.8**	**1.2**	**2.6**	**1.7**	2.6
2	*0.30*	*0.44*	0.95	0.64	**0.95**	**2.0**	**1.4**	**2.0**	**4.4**	3.0	*4.4*
1	0.74	1.1	**2.4**	1.6	**2.4**	**5.2**	**3.5**	**5.2**	11	*7.4*	*11*
5	1.9	2.8	**6.0**	4.0	**6.0**	**13**	**8.7**	**13**	28	*19*	*28*

[a]Λ, the divide slope parameter, represents a scale estimate of the slope transverse to the divide at a distance one ice thickness from the divide. The temperatures (0, −10, −30, −55)°C represent rate factors in proportion (1, 0.1, 0.01, 0.001); a in units of meters per year. Italic values indicate very unlikely parameters combinations, and bold values represent commonly found parameter combinations. The mean slope transverse to the divide is $\Lambda^{n/(n+1)}$, the value is about 5×10^{-3} for the commonly found cases presented here.

where Λ is the slope magnitude and the quantities on the right-hand side represent typical values at the divide when the ice is in steady state. Typical values for this slope lie between 0.001 (thick ice, low accumulation rate) and 0.02 (thin ice, high accumulation). Table 1 gives a range of possible values as a function of the parameters. Here we have chosen a single activation energy rheology, with $A(\theta = 0) = 10^{-16}$ Pa^{-3} a^{-1} ($B = 1.08 \times 10^5$ Pa a$^{1/3}$), and taken the relative rate factor A at (−10, −30, −55) °C to be (10^{-17}, 10^{-18}, 10^{-19}) Pa^{-3} a^{-1} (or $B = (2.32, 5.00, 10.78) \times 10^5$ Pa a$^{1/3}$).

[23] A similar analysis has been presented by *Wilchinsky and Chugunov* [1997], who obtain a similar estimate of the slope parameter, and show that the velocity field pattern depends on the rheological index only. More details are given in Appendix A. We go beyond the analysis of *Wilchinsky and Chugunov* [1997] by considering the effects of along-ridge flow. *Wilchinsky and Chugunov* [1997] also point out that since the slope is small one may view the solution domain near the divide as rectangular to $O(\Lambda)$, and the upper surface kinematical boundary condition is

$$w + a = 0 \tag{15}$$

to the same order. The driving stress provided by the surface slope can be replaced by an equivalent horizontal body force. The scale analysis then shows that for a power law rheology and for a uniform B (or, more generally, for the same spatial pattern of variation of B) solutions for all H, a, B with error $O(\Lambda)$ may be generated using the scalings

$$\begin{aligned} (u_x, w) &= a^*(\hat{u}_x, \hat{w}), \\ e_{ij} &= \frac{a^*}{H^*}\hat{e}_{ij}, \\ (\tau_{ij}, \pi) &= 2B\left(\frac{a^*}{H^*}\right)^{\frac{1}{n}}(\hat{\tau}_{ij}, \hat{\pi}), \\ (x, z, H, s, b) &= H^*\left(\hat{x}, \hat{z}, \hat{H}, \hat{s}, \hat{b}\right), \end{aligned} \tag{16}$$

where $\pi = p - \rho_i g\,(s - z)$ is the dynamic pressure and where the careted quantities are obtained by solving the equations

$$\begin{aligned} \partial_{\hat{z}}\hat{\tau}_{xz} + \partial_{\hat{x}}\hat{\tau}_{xx} &= \partial_{\hat{x}}\hat{\pi} + \hat{\gamma}_x, \\ \partial_{\hat{x}}\hat{\tau}_{xz} + \partial_{\hat{z}}\hat{\tau}_{zz} &= \partial_{\hat{z}}\hat{\pi}, \\ \partial_{\hat{x}}\hat{u} + \partial_{\hat{z}}\hat{w} &= 0, \\ \hat{\tau}_{ij} &= 2\hat{\eta}\hat{e}_{ij}, \end{aligned} \tag{17}$$

and where

$$\hat{\eta} = B\hat{e}^{1/n-1},$$

with boundary conditions

$$\begin{aligned} \hat{\tau}_{xz}(1, x) &= 0, \\ \hat{\pi}(1, x) + \hat{\tau}_{xx}(1, x) &= 0, \\ \hat{u}(0, x) &= 0, \\ \hat{w}(0, x) &= 0. \end{aligned} \tag{18}$$

on the domain $0 \le \hat{z} \le 1$, $-\hat{L} \le \hat{x} \le \hat{L}$. This of course is simply a standard finite element solution for the divide region; one solution approximately generates all [*Wilchinsky and Chugunov*, 1997].

[24] Scale analysis may also be used to show that solutions where the y slope (along ridge slope) γ_y is nonzero may be parameterized by the slope ratio $\delta = \gamma_y/\Lambda$, in other words we can generate a family of solutions parameterized by δ from which the specific solutions may be generated using these same scale relationships. Moreover, as expected, when δ is small, then, to $O(\delta^2)$ the x and y direction momentum balance equations partially decouple, and in fact are only coupled through the strain rate invariant. The strain rate invariant is approximated by

$$\hat{e}^2 = \hat{e}_{xz}^2 + \hat{e}_{xx}^2 + \delta^2\left(\hat{e}_{yz}^2 + \hat{e}_{xy}^2\right) + O(\delta^4), \tag{19}$$

where we ignore terms of $O(\delta^4)$. The reasons for retaining second-order terms in the invariant only are discussed in Appendix A. The x momentum and z momentum balance equations remain the same as for plane flow, while the y momentum balance equations for uniform thickness become

$$\partial_{\hat{z}}\hat{\tau}_{yz} + \partial_{\hat{x}}\hat{\tau}_{yx} = \hat{\gamma}_y, \tag{20a}$$

with

$$\hat{e}_{yz} = \frac{1}{2}\partial_{\hat{z}}\hat{u}_y, \quad \hat{e}_{xy} = \frac{1}{2}\partial_{\hat{x}}\hat{u}_y. \tag{20b}$$

where $\hat{\pi}$ is obtained from the x direction solution. For a power law rheology this is a nonlinear Poisson equation. For nonuniform thickness there is a contribution from $\partial\hat{\pi}/\partial\hat{y}$ (see Appendix A).

[25] In brief, divide flow is parameterized by two quantities, Λ and δ, and the dynamic fields are self-similar and can be derived from one solution by simple scalings. More generally, the viscous prefactor B varies with position, principally owing to temperature dependence, but in the divide area, as a consequence of the Raymond effect, the effect of this on the viscosity is less than that caused by

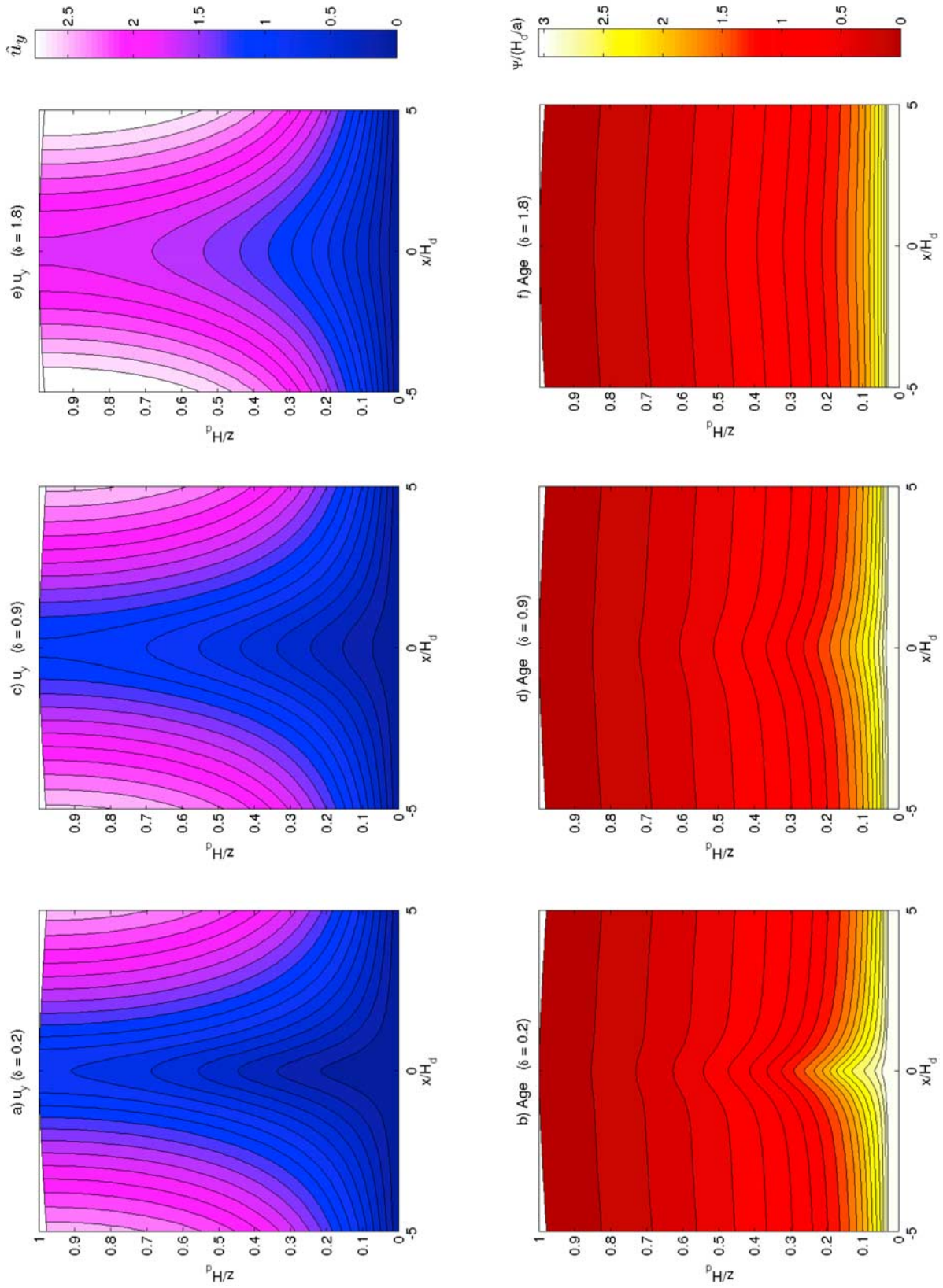

Figure 2. Contours of (a, c, e) along-ridge velocity v and (b, d, f) age Ψ for different values of the along-ridge slope ratio δ.

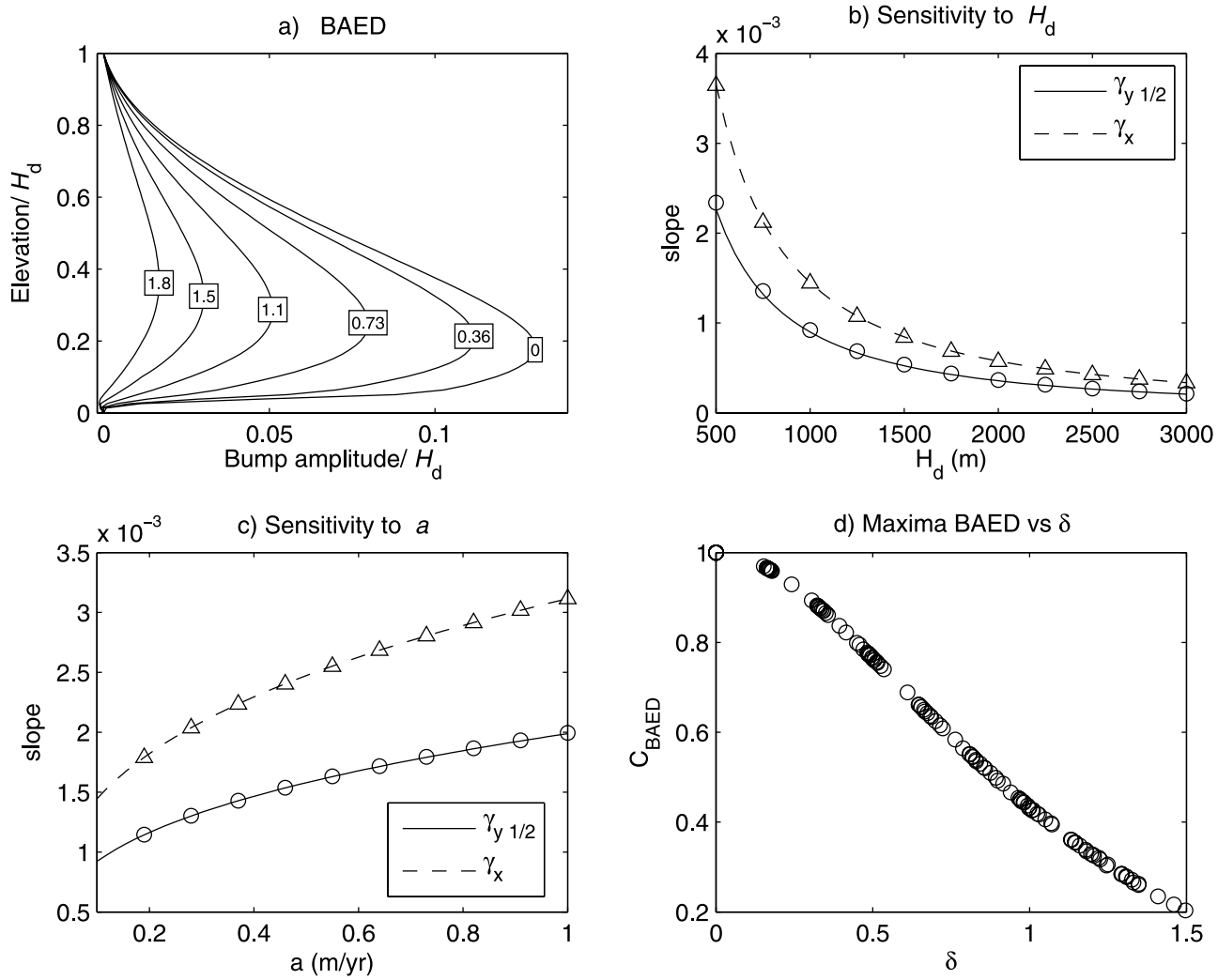

Figure 3. Sensitivity of Raymond effect to along-ridge flow. (a) BAED for different values of along-ridge slope ratio δ. (b and c) Sensitivity of $\gamma_{y(1/2)}$ and γ_x to divide thickness and accumulation rate. Lines represent the sensitivity predicted by the scaling, and symbols represent the results of the numerical model (solid lines and circles for $\gamma_{y(1/2)}$, dashed lines and triangles for γ_x). (d) Dependence of the bump amplitude with δ (C_{BAED} is the maximum bump amplitude relative to the case without along-ridge flow).

the variation in the strain rate invariant. Thus, even though the distribution of B varies as one changes Λ and δ, the change in this is small compared with the change in the strain rate invariant, so thermoviscous coupling is not a dominant process in the Raymond effect, although it does have a discernible quantitative effect [*Martín et al.*, 2006]. Finally, when the geometry does not change in the y direction, (19) and (20) are exact as the y gradients are zero.

3. Physics of the Raymond Effect

[26] Here we consider the influence of (1i) along-ridge flow and (2) sliding on the Raymond effect. The latter has been considered previously by *Pettit et al.* [2003], who restricted their study to a linear sliding law ($m = 1$ in equation (4)). Either of the above processes is capable of reducing the magnitude of the Raymond effect and thus Raymond Bumps, which will influence ice history studies.

[27] To aid quantitative discussion, we define BAED as the bump amplitude versus elevation distribution and BWED as the bump width versus elevation distribution. BAED is measured by comparing the full Stokes with SIA isochrones. BWED is the horizontal distance between the points where the separation between full Stokes and SIA isothermal isochrones is half the maximum bump amplitude of the full Stokes isochrones. This is somewhat arbitrary but seems to provide an informative descriptor.

3.1. Effect of Along-Ridge Flow

[28] In this section we assume that the along-ridge velocity and surface gradients are negligible or that the slope in the along flow direction is small, that is, the slope ratio δ is smaller than one. In the former case the simplification of the momentum balance (2) we use in this section is exact and in the latter is an approximation $O(\delta^2)$.

[29] Following the analysis summarized in section 2.3, we decouple the momentum balance equations in the (x, z)

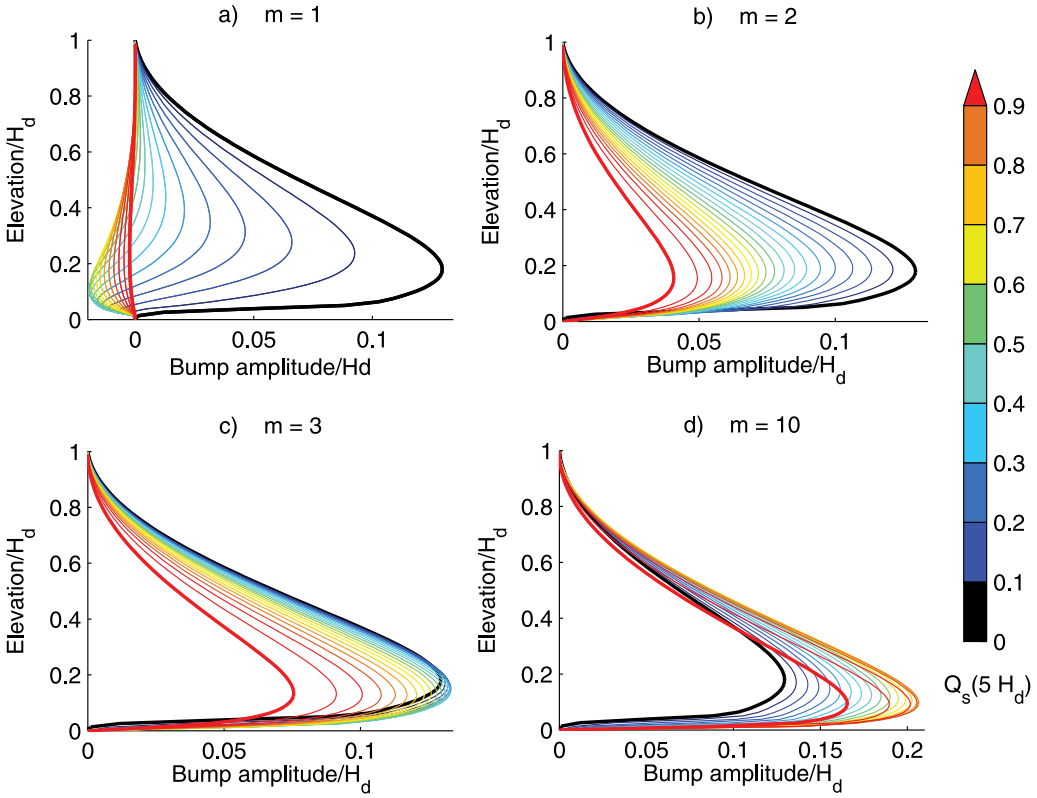

Figure 4. BAED for different values of fraction of flux due to sliding ($Q_s(5\ H_d)$) at selected values between 0 and 0.95 (black to red); different values for different indices in the sliding law are shown: (a) $m = 1$, (b) $m = 2$, (c) $m = 3$, and (d) $m = 10$. The black thick line ($Q_s(5\ H_d) = 0$) represents ice frozen to the bed and it is identical in Figures 4a–4d. Note that for linear sliding, the bump amplitude decreases with sliding; the depressions for linear sliding are not a numerical artifact but have a physical meaning. For nonlinear sliding with $m > n$ the dependence on bump amplitude is nonmonotonic. See text for explanation.

direction and the y direction, using the strain rate invariant (19), and approximating the y momentum balance equation with (20). We solve (20) and the momentum conservation in the (x, z) plane iteratively using a fixed point scheme. The nonuniform thickness equivalent is given in Appendix A.

[30] We illustrate how along-ridge flow affects the flow at divides in Figures 2 and 3. Along-ridge flow reduces the Raymond effect because stresses are increased in the stagnant core of the divide in the lower part. Figure 2 shows along-ridge velocity and isochrones as the along-ridge slope ratio δ increases (Figure 2). For low slopes, the along-ridge flow is strongly modulated by the stagnant zone, meaning that the along-ridge flow in this zone is small. Moving away from the divide, the flow transverse to the ridge causes the viscosity at the base to decrease, and the along-ridge flow to increase. This modulation occurs even when the Raymond effect is so small that Raymond bumps are scarcely discernible (Figures 2e and 2f).

[31] The dependence of BAED with slope in the along-ridge direction is plotted in Figure 3a. The slope ratio δ in the along-ridge direction has to be significant in order to impede the formation of bumps ($\delta = \gamma_y/\Lambda \gtrsim 1$). For $\delta = 1$ the slope in the x direction is smaller than the along-ridge slope until a distance of the ice divide of about the ice thickness. Note that even though $\delta = O(1)$, this solution is accurate as we have imposed no y gradients in the velocity field.

[32] The scaling makes predictions about the dependence of results on the model parameters with error $O(\Lambda)$. Defining $\gamma_{y(1/2)}$ as the along-ridge slope which reduces the maximum bump amplitude by half compared with the case with no transverse flow, the scaling relations show that both

$$\left(\gamma_{y(1/2)},\ \gamma_x\right) \propto \Lambda \propto \frac{a^{*\frac{1}{n}}}{H^{*\frac{1}{n}+1}}. \tag{21}$$

Figures 3b and 3c show that these relations hold to a very good approximation. This implies that the bump size should only depend upon δ for fixed n (where there is no sliding) which is shown in Figure 3d, which combines results from the parameter values selected in Figures 3b and 3c.

[33] The value of $\delta_{(1/2)}$, the slope ratio corresponding to $\gamma_{y(1/2)}$, is independent of the parameters (i.e., a and H_d) as expected from the scaling. The transverse slope ratio necessary to halve the bump amplitude is $\delta_{(1/2)} = 0.888 \pm 0.002$ in the experiments shown in Figure 3.

3.2. Influence of Sliding on the Operation of the Raymond Effect

[34] Since the Raymond effect is a consequence of internal deformation, one is naturally led to inquire as to

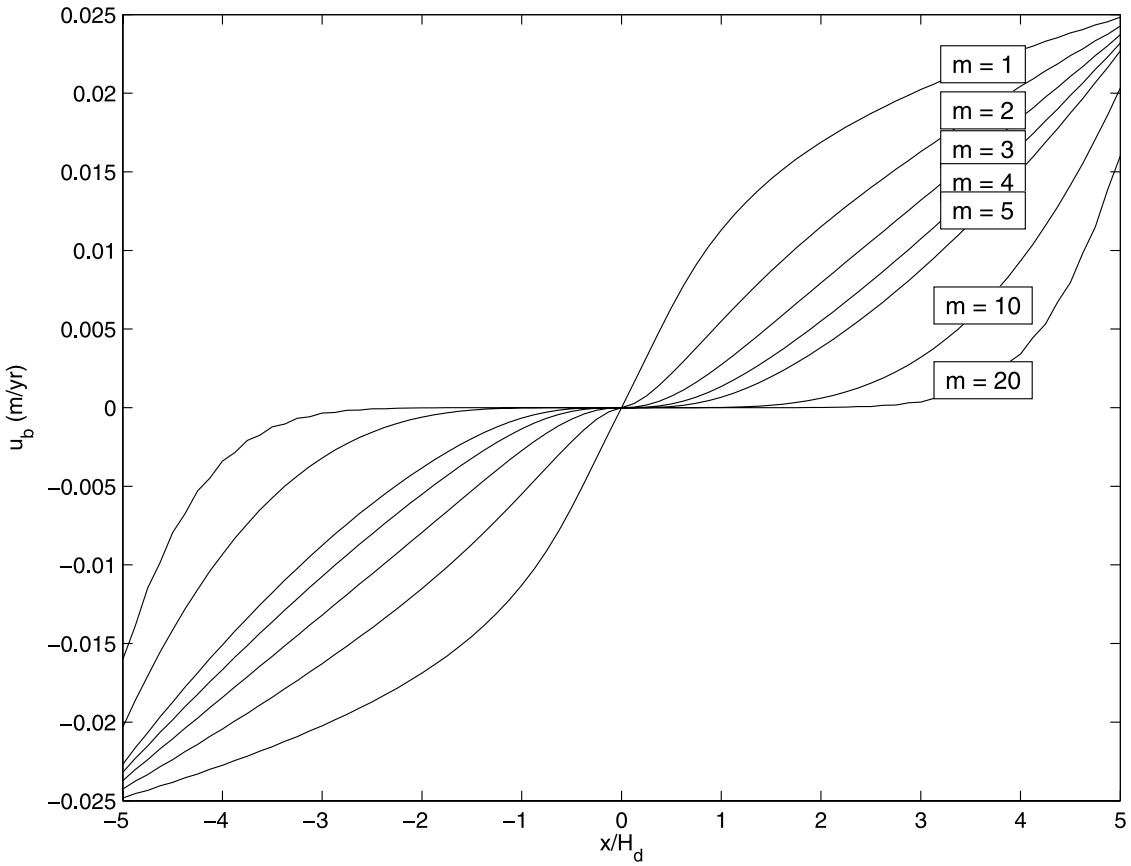

Figure 5. Basal velocities for sliding index $m = \{1, 2, 3, 4, 5, 10, 20\}$ and sliding flux ratio $Q_s = 0.05$.

whether sliding will reduce the magnitude of Raymond Bumps. To investigate this, we model the basal sliding using a Weertman relation with index m (equation (4)). The magnitude of sliding is expressed through the sliding flux ratio, which is defined as the fraction of the horizontal flux (Q_s) due to sliding [*Pettit et al.*, 2003]

$$Q_s(x) = \frac{u_x^{(b)}(x)H(x)}{Q(x)}, \tag{22}$$

evaluated at a distance of five times the ice divide thickness. In Figure 4 we show the bump amplitude versus elevation distribution (BAED) assuming four values of the sliding index (m = 1, 2, 3 and 10). Each plot shows the BAED for different proportions of sliding flow expressed in terms of the flank sliding flux ratio Q_s.

[35] For linear basal sliding (m = 1) we obtain similar results to those shown by *Pettit et al.* [2003], except near the divide bottom, where we find that the isochrones are downwarped (i.e., form synclines). This is because the sliding viscosity (i.e., $1/(C|\boldsymbol{\tau}_t^{(b)}|^{m-1})$ in equation 4), which in this case is not stress-dependent, remains small, while the ice viscosity becomes very large as one approaches the divide. Thus, approaching the divide, ice flow becomes progressively transferred from deformation within the ice to sliding, which creates a nearly plug flow and deeper penetration of ice flow and isochrones to the bed. This feature is not given by *Pettit et al.* [2003] because they interpolate the BAED close to the base of the divide.

[36] When the basal sliding is nonlinear but the index m remains smaller than the ice rheological index n = 3 (represented by m = 2 in Figure 4), the effect of basal sliding is, as in the linear case, to reduce the Raymond effect although by a lesser amount compared with a linear sliding rheology. The same argument as above holds; when the shear stress becomes small near the divide, the ice viscosity increases faster toward the divide than the sliding viscosity, and flow is progressively transferred to sliding. However, even when very high basal flux ratios are considered ($Q_s(5H_d)$ = 0.95 in Figure 4) the Raymond effect is not entirely eliminated. Thus, although we have not made an attempt to make the synclines apparent for nonlinear rheologies with $m < 3$, in principle such synclines might indeed appear.

[37] When higher-index nonlinear sliding is considered the behavior becomes slightly nonintuitive. For $m > 3$ the sliding proportion increases with shear stress faster than the ice viscosity, meaning that motion is transferred from internal deformation to sliding as one moves from the divide, and sliding velocity near the ice divide (see Figure 5) becomes smaller as m is increased. One would therefore expect maximum bump amplitudes to be comparable with those for the case of no slip (Q_s = 0). However, the former are greater; for example, in our experiments, if $m \geq 3$ the bump amplitude increases with sliding proportion until a

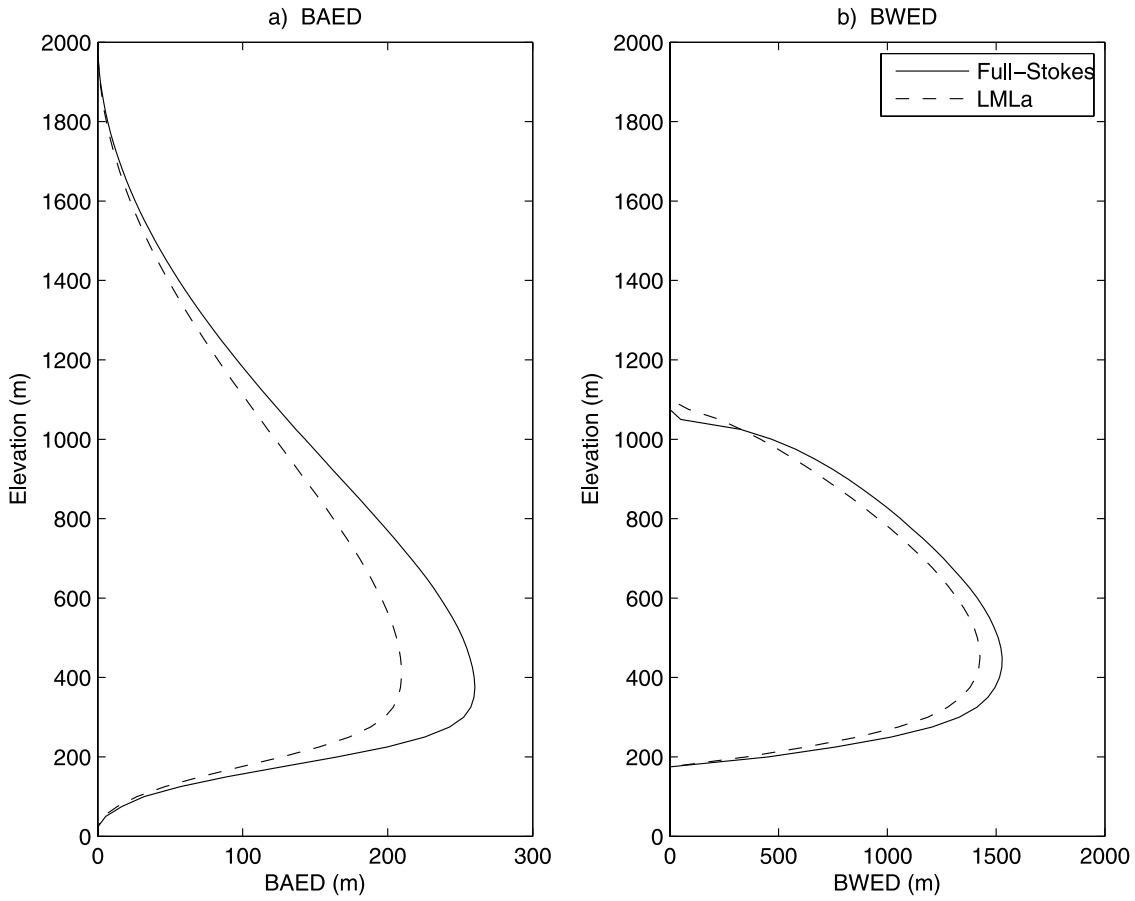

Figure 6. Steady (a) BAED and (b) BWED for full Stokes (solid line) and LMLa models (dashed line). H_d = 2000 m and a = 0.2 m a^{-1}.

certain basal flux ratio Q_s is reached; thereafter the bump amplitude decreases sharply with the sliding but is never damped to zero. (See Figure 4, m = 3 and 10.)

[38] The reason for this is not so much that the flow near the divide is affected, but has more to do with the fact that as sliding proportion increases away from the divide, the flow becomes more plug-like, causing isochrones in the flanks to be lower (see *Parrenin and Hindmarsh* [2007] and *Leysinger Vieli et al.* [2007] for further discussion on this). This lowering in the isochrones at the flanks causes the bump amplitude to be larger. However, as the sliding proportion increases, the area of flow immediately adjacent to the divide that is unaffected by sliding becomes smaller. This reduction causes the Raymond bumps to become smaller. This effect of bump amplitudes increasing compared with the case of no slip is most noticeable for small basal sliding ratios although it becomes more important as the sliding index m is increased.

3.3. Longitudinal Stresses and the Raymond Effect

[39] The numerical models that include horizontal gradients of longitudinal stresses, even if they do not solve the full Stokes system of differential equations (1)–(2) qualitatively reproduce the Raymond effect [*Blatter*, 1995; *Saito et al.*, 2003; *Pattyn*, 2003]. We use an isothermal model essentially similar to those (see a formal description in the work by *Hindmarsh* [2004], LMLa models) to compare them with the full Stokes model described in this paper (section 2.1). Both models are solved by means of the same numerical scheme (details in the Appendix B).

[40] In Figure 6, BAED and BWED are shown for both models for a typical sample case (H_d = 2000 m, a = 0.2 m a^{-1}). The shape of the curves is quite similar but for the higher-order LMLa model the bumps have a smaller amplitude compared with the full Stokes solution. Note that the discrepancies appear in the bump amplitude (typically 25%) rather than in the bump width (difference less than 5%). These discrepancies could be understood as a measure of error of the LMLa models, as the full Stokes model includes all the stress components in the force balance.

[41] It is straightforward to show that the scale analysis presented in section 2.3 holds for the Blatter model; in consequence we do not expect the difference between full Stokes and LMLa models to depend strongly on the parameters (i.e., a and H).

4. Signals of Divide Motion

[42] Numerically, we can force the steady state position of the ice divide (x_d^f) by adjusting the outgoing ice flux at the divide flanks where we impose global mass conservation.

$$Q(x) = \int_b^s u_x(x, z')\mathrm{d}z' = \int_{x_d^f}^x (a(x') - \chi)\mathrm{d}x', \qquad (23)$$

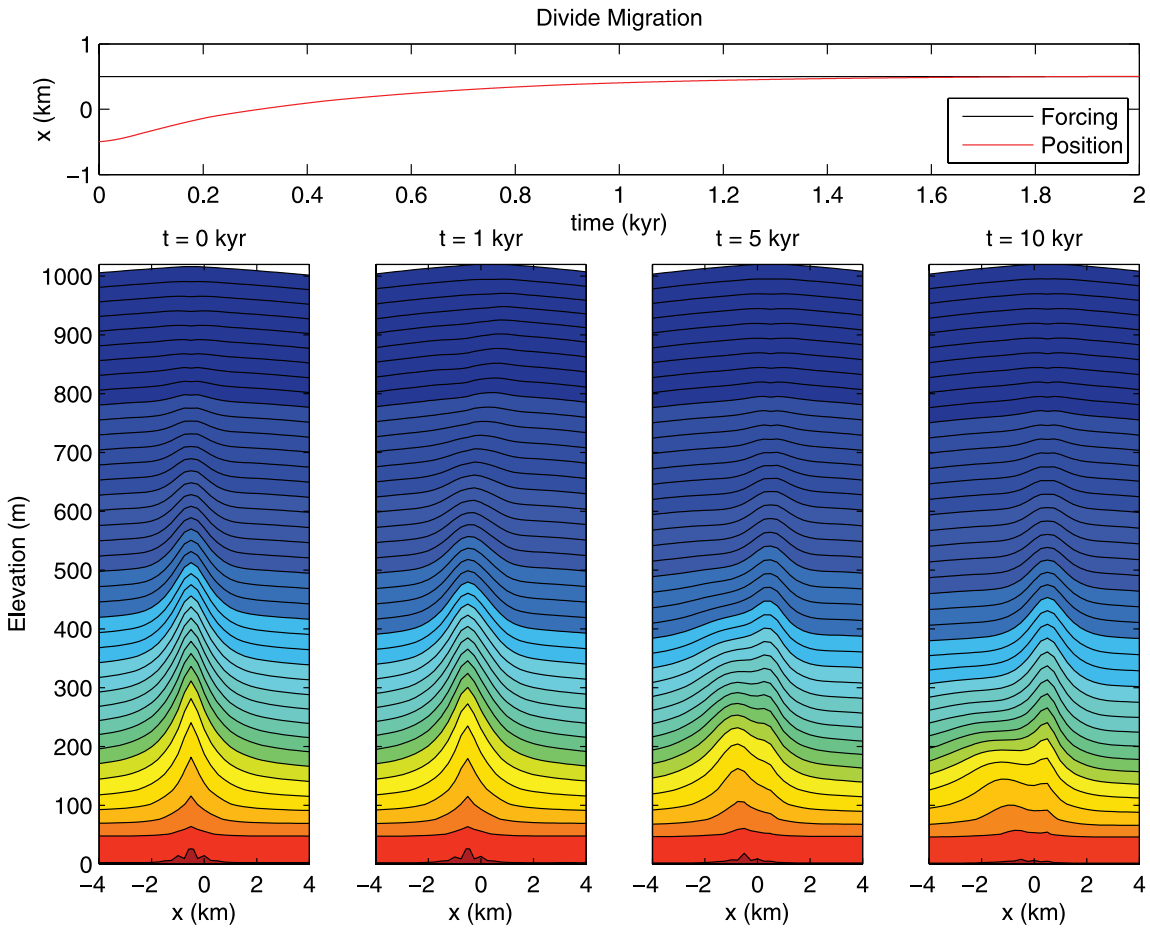

Figure 7. Effect of a fast divide migration on the radar layers. Initially, the divide is in a steady configuration and a instantaneous migration of 1 km is forced. (top) Evolution of the divide position with time and (bottom) the contours showing four stages ($t = \{0, 1, 5, 10\}$ ka) of the ice stratigraphy evolution. $H_d = 1000$ m and $a = 0.1$ m a^{-1}.

where χ is the thinning rate. If we let the system evolve, the ice divide position (x_d) will progressively shift to the new steady state position which we are forcing by mass conservation (x_d^f). Constraining the output flux thus corresponds to altering the back stress [*Schoof*, 2007].

[43] Previous transient models of ice divides considered the temperature field to be in instantaneous steady state so that the time derivative in equation (6) is neglected [*Nereson and Waddington*, 2002; *Martín et al.*, 2006]. However, the characteristic response time for temperature to a given perturbation is larger than the response time appropriate to surface geometry [*Nereson and Waddington*, 2002]. In consequence, in this paper we consider the transient response of temperatures during divide migration. This typically results in a stronger asymmetry in the isochrones compared with the isothermal case, owing to the retarded response of the temperature field compared with the surface geometry. This effect is particularly noticeable when fast divide migrations are involved.

4.1. Fast Migration of the Divide Position: Raymond Bumps Asymmetry

[44] Starting with the stationary velocities, age and temperature fields for an ice divide, we numerically force the migration of the ice divide to a new position where it becomes again stationary.

[45] Figure 7 illustrates the effect of this instantaneous migration on the ice stratigraphy. Arched layers beneath the new ice divide position are developed while those previously formed at the ancient position are attenuated and advected away from the divide. This produces a strong asymmetry in the radar stratigraphy beneath the divide.

[46] Figure 7 also shows the evolution of the divide position with time. *Hindmarsh* [1996] showed that the divide position decays stably to the new stationary position. Moreover, for small amplitudes of migration, the divide position decays exponentially with a time constant for divide relaxation 16 times smaller than the H_d/a timescale for ice sheets. In the experiment shown in Figure 7, $H_d/a = 10$ ka. The fast migration does not affect this surface kinematic result but does affect the layer architecture.

4.2. Slow Migration of the Divide Position: Tilted Raymond Bumps

[47] Where the rate of divide migration is sufficiently slow (compared with the time of divide relaxation) the Raymond bumps are not abandoned, producing a relict set

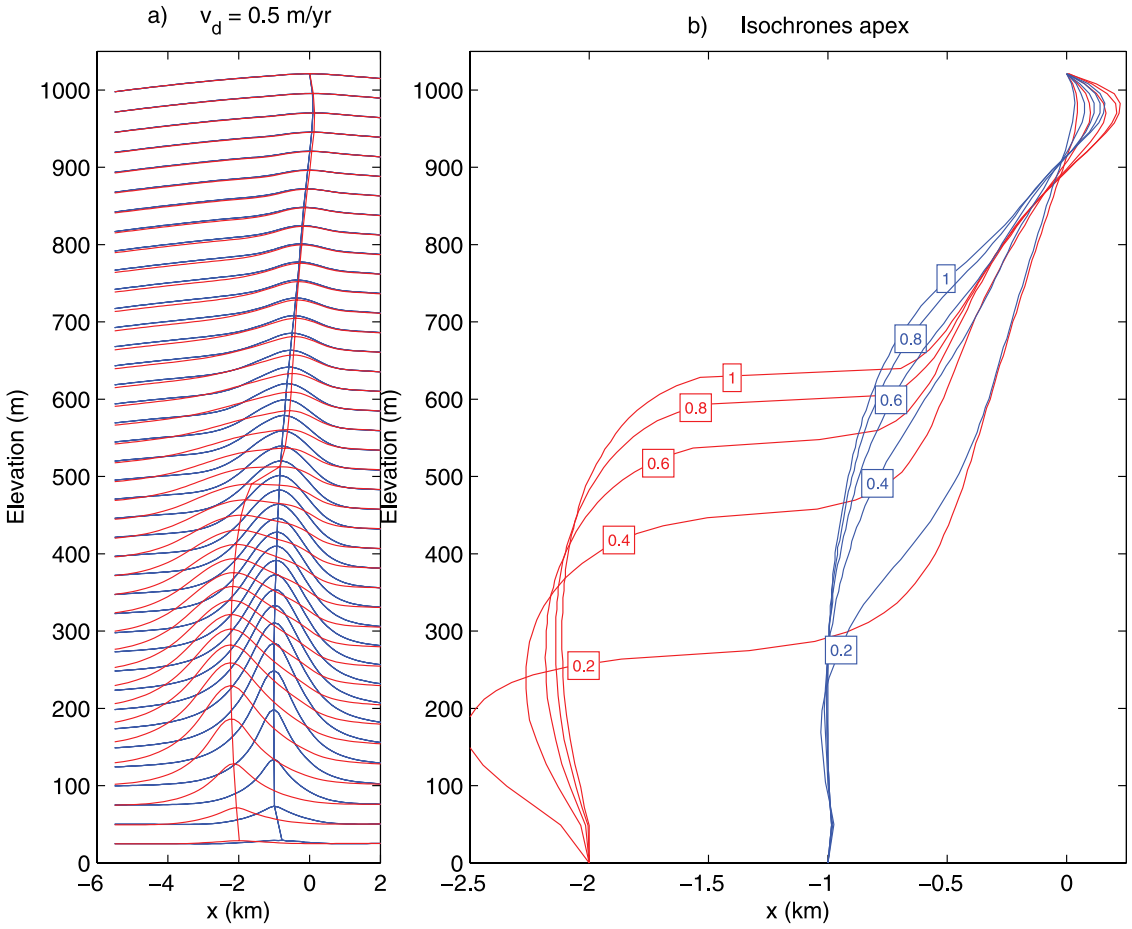

Figure 8. (a) Isochrones at present time after a divide migration of 1 km (blue lines) and 2 km (red lines) at constant rate ($v_d = 0.5$ m a^{-1}). (b) Locus of apex crests after divide migration of 1 km (blue lines) and 2 km (red lines) at different rates (v_d = {0.2, 0.4, 0.6, 0.8, 1} m a^{-1}). Elapsed times since start of migration depend upon migration rate.

and a new set, but form instead a tilted stack with the base corresponding to the former position. Such a tilted stack has been observed at Siple Dome [*Nereson et al.*, 1998b]. To simulate the progressive advance of the ice divide, we change the forced divide position (equation (23)) at a constant rate v_d.

[48] Figure 8a shows the isochrones after a divide migration. Two cases are considered, one with a small migration (one ice thickness horizontal displacement), the other with a larger migration (two ice thicknesses). The upper isochrones are very similar for the two cases, particularly the isochronal apex position, while the bottom isochrones are essentially the relict Raymond bumps.

[49] In Figure 8b the previous results are extended to different values of the rate of migration but for brevity only the positions of the isochrone apexes are shown. For the large migration case, where there are clear relict bumps being advected away by the flow and new bump stacks, the position of the bump apex shows a jump at a certain elevation as a result of its definition. For displacements somewhere between one and two ice thicknesses, a situation with both an old and a new bump stack becomes apparent.

4.3. Stochastic Forcing of Divide Position

[50] We have seen in section 4.1 that following an instantaneous ice divide migration the original Raymond arches are spread out. If an ice divide varies its position several times this mechanism can severely attenuate the cumulative action of the Raymond effect. In order to simulate a stochastic movement of the ice divide we prescribe, at each time interval Δt_d, a new random target steady state position of the ice divide x_d^f by adjusting the flank fluxes (equation (23)). We then let the system evolve during the interval Δt_d. For simplicity we consider Δt_d constant and x_d^f a random variable, uniformly distributed in $[-(x_d^f)_{\max}, (x_d^f)_{\max}]$ (see Figure 9).

[51] If the time Δt_d is large compared with the time constant for divide relaxation (section 4.1) the Raymond bump amplitude depends principally on the time during which the divide was located at any particular spot. We are more interested here in the effect of fast divide stochastic migrations on the Raymond curves, and then the time Δt_d has consequently been chosen to be small (0.1 ka) compared with the H_d/a advection timescale (H_d/a = 10 ka) for Raymond bump formation [e.g., *Hindmarsh*, 1996; *Waddington et al.*, 2005].

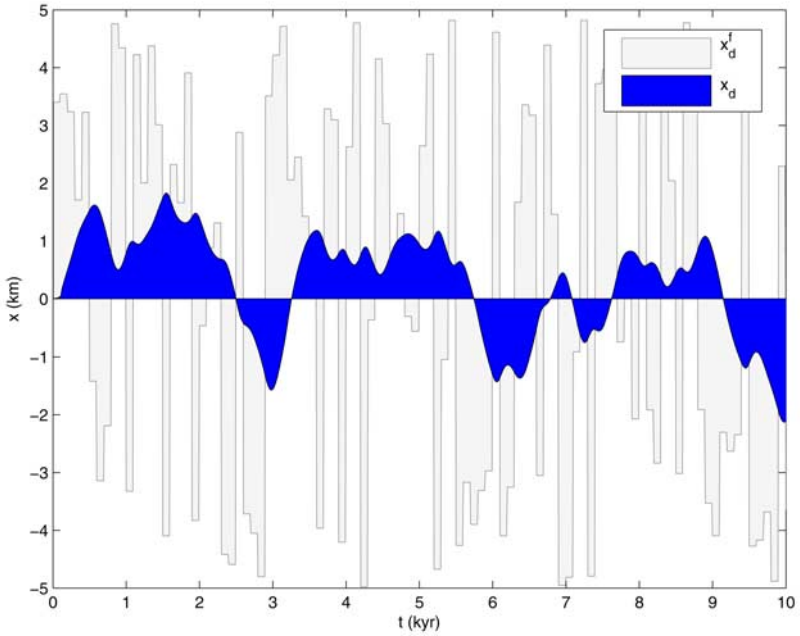

Figure 9. Position of the ice divide x_d (blue) subjected to stochastic variation. The forcing is plotted by showing the target divide position x_d^f (grey) at each time step. The new random target divide position is prescribed every 0.1 ka (Δt_d = 0.1 ka) and is uniformly distributed in the interval [−5, 5] km ($(x_d^f)|_{\max}$ = 5 km). The H_d/a advection timescale is 10 ka.

[52] To present the results we have averaged BAED and BWED over several runs (50 runs, each of 10 ka). Figure 9 shows the evolution of the divide position and the forced divide position for one of the runs. In Figure 10 the main results are presented. As the amplitude of the migration becomes greater, the Raymond bumps are shallower and are more spread. The largest amplitude used for the target divide position ($(x_d^f)_{\max}$ = 5 km) produces a stochastic divide migration with breadth comparable to the ice thickness (see Figure 9) and, in this case, the Raymond bump amplitude is reduced considerably (to 20%) and the Raymond bumps are spread within an area nearly twice wider than the unperturbed one (see BAED and BWED in Figure 10).

[53] The BAED looks similar to the one that might be obtained where the bumps were newly formed (Figure 11); in other words, it seems that there is a possibility that stochastic behavior could be misinterpreted. However, the bumps are much more spread out, which indicates that measuring bump width is important in determining whether undersized bumps are due to stochastic effects or to youth. In interpreting these results it should be stressed that they are averages of many runs and may not correspond to individual instances of the stochastic process.

5. Discussion: Interpretation of the Raymond Effect

[54] Bump architecture has been used to infer changes in ice thickness and ice geometry (see section 1 for a list of references). In this section, we consider how the insights gained in this paper affect our interpretation. How might the various influences: along-ridge flow, sliding, divide migration slow, fast and stochastic affect our interpretations of Raymond bump geometry? In particular, we are interested in how ignoring these effects might affect the Raymond bump geometry, leading us to erroneous conclusions when inferring ice thickness history.

[55] A simple but important point is that the scale analysis justifies the *ad hoc* procedure used by *Conway et al.* [1999], who parameterized the velocity fields using a shape function procedure. The scale analysis shows that the assumption that the shape function is constant is valid with accuracy $O(\Lambda)$.

[56] In steady state, the maximum bump amplitude and corresponding elevation are determined by the rheological index and for anisotropy. If the observed bump amplitude is oversized, with respect to the steady state, this can be because the ice has thinned [*Conway et al.*, 1999], because the rheological index is greater than we imagined, or because of a limited amount of sliding. An indication of whether sliding might be occurring can be obtained by computing the basal temperature. The surface profile depends on the rheological index, and this can be used to distinguish between hypotheses to a certain extent.

[57] If the bump amplitude is undersized with respect to the expected steady state value, this can also be due to an incorrect assumption regarding the rheology, and the above comments apply. It can be due to the ice thickening, in which case the elevation of maximum amplitude will be lower than expected, or it can be because the bump is juvenile, in which case the elevation of maximum amplitude is higher than expected. A third possibility is weakening of the Raymond effect due to along-ridge flow; Figure 11 indicates that in this case, the elevation of maximum amplitude does not depend strongly on the along-ridge

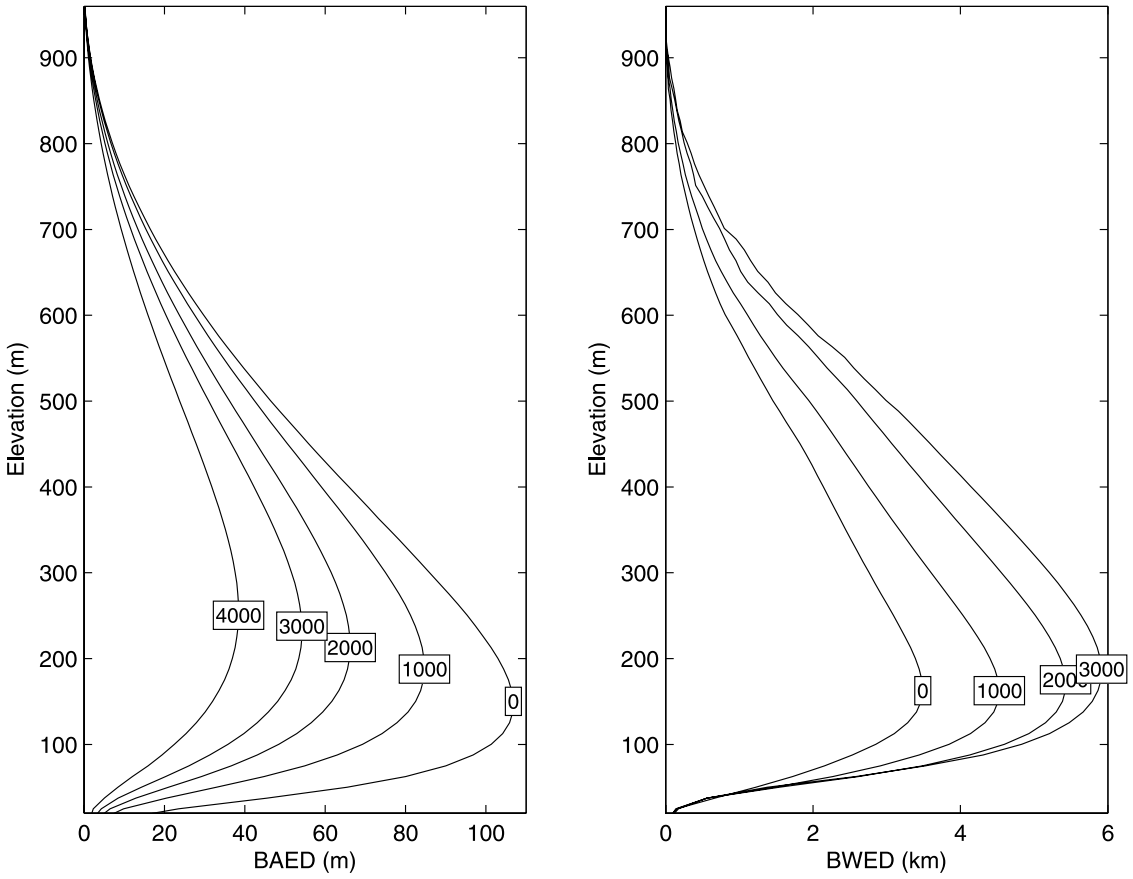

Figure 10. BAED and BWED after stochastic forcing of divide position for different values of $(x_d^f)|_{\max}$. Averaged over 50 runs of 10 ka.

slope, and this is also true when sliding affects the flow around the divide. Figure 11 also shows that the elevation of maximum amplitude does depend upon age, while divide motion decreases the bump amplitude, but can be distinguished from the effects mentioned above by the broadening of the bump stack.

6. Conclusions

[58] In this study, we explore the effect of divide migration, along-ridge flow and basal sliding on the layer architecture. We find the following:

[59] 1. Along-ridge flow reduces and can eliminate the Raymond effect through the contribution of along-ridge strain rates to the strain rate invariant, reducing the viscosity near the base of the ice under the divide. The ratio of ridge-parallel and ridge-transverse slopes (at a distance of one ice thickness from the divide) has to be relatively large (0.9) to reduce the size of steady Raymond bumps by one half.

[60] 2. We have extended the discussion of *Pettit et al.* [2003] by showing how the effect of basal sliding on Raymond bumps depends on the relative magnitudes of the stress/traction indices for sliding and for internal deformation. If the sliding index is less than the deformation index, sliding can dominate near the divide and the Raymond effect will not be apparent. In fact, if internal deformation becomes significant in the flank area, one can find depressions in the basal radar layers as a consequence of the plug flow induced by sliding. In contrast, if the sliding index is larger or equal than the internal deformation index, then sliding will become insignificant near the divide, and we expect to see Raymond bumps forming.

[61] 3. There are a set of mechanical approximations to the stress equations intermediate between the shallow ice approximation and the Stokes equations termed "higher-order models" [*Blatter*, 1995]. Such models produce bumps, but there are significant quantitative errors in bump amplitude which render these models unable to extract flow history information from radar layers near the ice divide.

[62] 4. Tilted Raymond bump stacks can be used to extract information of past divide migration [e.g., *Nereson et al.*, 1998b]. There is a sharp transition between isochrones affected and unaffected by the divide migration, i.e., the apexes of the isochrones are not in a straight line: the upper isochrones contain information of the rate of migration and bottom layers about the former position of the divide.

[63] 5. Fast stochastic divide migrations, by delocalizing the operation of the Raymond effect, also reduce and can even eliminate the formation of Raymond bump stacks.

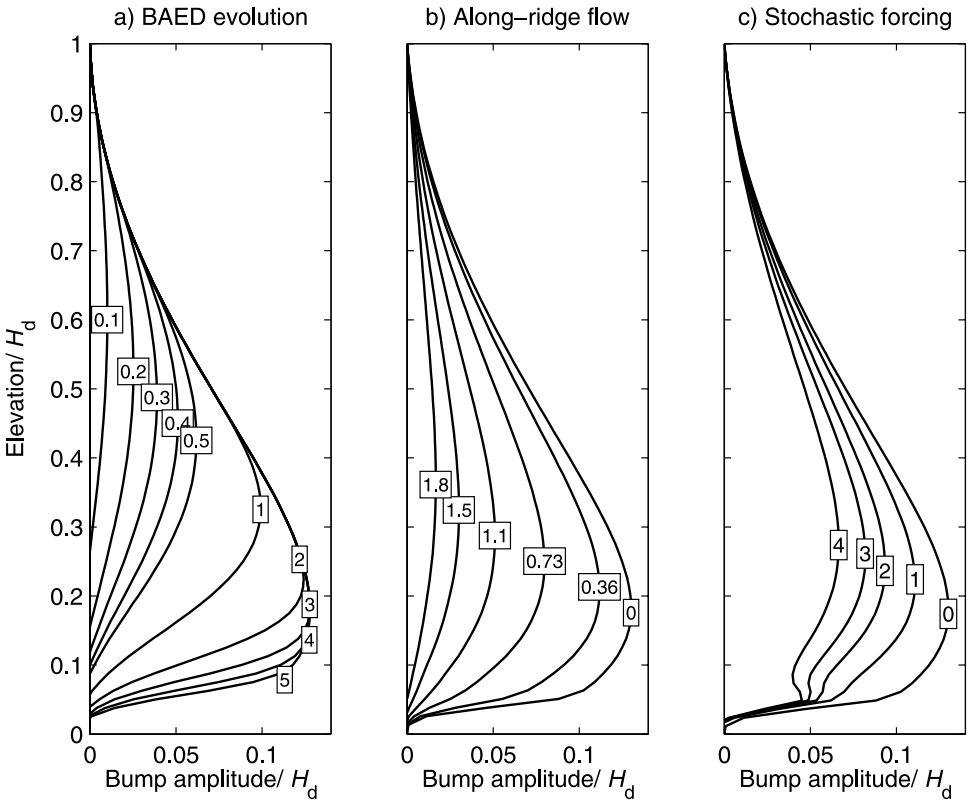

Figure 11. Comparison of the effect on the BAED of the evolution of the ice divide stratigraphy, the along-ridge flow, and the stochastic forcing of the divide position. (a) BAED at different stages of the transient simulation $t = \{0.1, 0.2, 0.3, 0.4, 0.5, 1, 2, 3, 4, 5\}$ dimensionless time units (this is given by H_d/a, i.e., the advection time of the divide), (b) BAED for different values of along-ridge slope ratio $\delta = \{0, 0.36, 0.73, 1.1, 1.5, 1.8\}$, and (c) BAED after stochastic forcing of divide position for different values of $(x_d^f)|_{\max}$ ($(x_d^f)|_{\max} = \{0, 1, 2, 3, 4\}\ H_d$).

[64] 6. Fast divide migrations result in the appearance of both new and relict bump stacks, while slower migrations results in tilted bump stacks.

[65] 7. Following *Wilchinsky and Chugunov* [1997], a scale analysis shows that divides can be characterized by one parameter,

$$\Lambda \equiv \frac{2B}{\rho_i g H^*}\left(\frac{a^*}{H^*}\right)^{\frac{1}{n}}$$

which is also the order of magnitude of the slope at a distance of one ice thickness away from the divide. Typical values lie between 0.0008 (e.g., Dome C area) to 0.02 (e.g., Fletcher Ice Rise). We also show that when there is flow along the divide ridge, a second parameter, δ, the ratio of the along-ridge slope γ_y to Λ is needed to characterize the flow. Again, having computed the solution for one δ and one distribution of B permits generation of the solution for all other combinations of a, H and B.

Appendix A: Scale Analysis of Divide Solutions

[66] We restrict consideration to frozen beds which are flat in the x direction but may have uniform slope in the y direction, mainly for reasons of brevity. The analysis here could in principle be extended to include these cases. In two dimensions the Stokes equations are

$$\begin{aligned} \frac{\partial \tau_{xz}}{\partial z} + \frac{\partial \tau_{xx}}{\partial x} - \frac{\partial \pi}{\partial x} &= \rho_i g \gamma_x, \\ \frac{\partial \tau_{xz}}{\partial x} + \frac{\partial \tau_{zz}}{\partial z} - \frac{\partial \pi}{\partial z} &= 0, \end{aligned} \tag{A1}$$

where γ_x is the slope in the x direction, $\pi = p - \rho_i g(s - z)$ is the dynamic pressure and

$$\tau_{ij} = 2Be^m e_{ij}, \qquad \left(m = \frac{1}{n} - 1\right)$$

where this definition of m is used in this appendix. We scale distances by H^*, strain rates by a^*/H^* and stresses by $2B\left(\frac{a^*}{H^*}\right)^{\frac{1}{n}}$

$$\begin{aligned} (u, w) &= a^*(\hat{u}, \hat{w}), \\ e_{ij} &= \tfrac{a^*}{H^*}\hat{e}_{ij}, \\ (\tau_{ij}, \pi) &= 2B\left(\tfrac{a^*}{H^*}\right)^{\frac{1}{n}}(\hat{\tau}_{ij}, \hat{\pi}), \\ (x, z, H, s, b) &= H^*\left(\hat{x}, \hat{z}, \hat{H}, \hat{s}, \hat{b}\right), \end{aligned} \tag{A2}$$

and the slope is scaled by

$$\gamma_x = \Lambda\hat{\gamma}_x, \quad \Lambda = \frac{2B}{\rho_i g H^*}\left(\frac{a^*}{H^*}\right)^{\frac{1}{n}} \ll 1, \tag{A3}$$

where the dimensionless parameter $\Lambda \ll 1$ represents a slope magnitude at a unit distance (one ice thickness from the divide). Typically, Λ lies between 0.001 and 0.02.

[67] We also use the fact that slopes are small near the divide and approximate, by solving in the domain $0 \le \hat{z} \le 1$, arriving at the equations

$$\begin{aligned} \frac{\partial\hat{\tau}_{xx}}{\partial\hat{x}} + \frac{\partial\hat{\tau}_{xz}}{\partial\hat{z}} - \frac{\partial\hat{\pi}}{\partial\hat{x}} &= \hat{\gamma}_x + O(\Lambda), \\ \frac{\partial\hat{\tau}_{xz}}{\partial\hat{x}} + \frac{\partial\hat{\tau}_{zz}}{\partial\hat{z}} - \frac{\partial\hat{\pi}}{\partial\hat{z}} &= 0. \end{aligned} \tag{A4}$$

[68] The boundary conditions are

$$\begin{aligned} \hat{\tau}_{xz}(1,x) &= 0, \\ \hat{\pi}(1,x) + \hat{\tau}_{xx}(1,x) &= 0, \\ \hat{u}(0,x) &= 0, \\ \hat{w}(0,x) &= 0. \end{aligned} \tag{A5}$$

By adjusting $\hat{\gamma}_x$ as a function of $\hat{x}$ we can satisfy the steady state surface kinematic condition

$$\hat{w}(1) = 1 + O(\Lambda).$$

For a power law rheology with uniform rate factor, the field equations can be written as

$$\frac{\partial\hat{e}^m\hat{e}_{xx}}{\partial\hat{x}} + \frac{\partial\hat{e}^m\hat{e}_{xz}}{\partial\hat{z}} - \frac{\partial\hat{\pi}}{\partial\hat{x}} = \hat{\gamma}_x + O(\Lambda), \tag{A6}$$

and the equation sets contain only n as a parameter. In the present context, the significance of this is that we generate one solution for the velocity fields, then by descaling, we can generate solutions for all combinations of B, a^* and H^*.

[69] The plane flow has been considered by *Wilchinsky and Chugunov* [1997], who obtain the same results; the only difference is that they expand in the mean slope of the ice sheet (their ε, which we denote ε_{WC}), which is the usual expansion parameter in the shallow ice approximation. It is straightforward to show that $\Lambda = \varepsilon_{WC}^{n/(n+1)}$.

[70] In three dimensions the equations are

$$\begin{aligned} \frac{\partial\tau_{xx}}{\partial x} + \frac{\partial\tau_{xy}}{\partial y} + \frac{\partial\tau_{xz}}{\partial z} - \frac{\partial\pi}{\partial x} &= \rho_i g\gamma_x, \\ \frac{\partial\tau_{xy}}{\partial x} + \frac{\partial\tau_{yy}}{\partial y} + \frac{\partial\tau_{yz}}{\partial z} - \frac{\partial\pi}{\partial y} &= \rho_i g\gamma_y, \\ \frac{\partial\tau_{xz}}{\partial x} + \frac{\partial\tau_{yz}}{\partial y} + \frac{\partial\tau_{zz}}{\partial z} - \frac{\partial\pi}{\partial z} &= 0, \end{aligned} \tag{A7}$$

where

$$\gamma_y = \left(\frac{\partial s}{\partial y} - \frac{g_y}{g}\right),$$

and we have introduced a body force g_y in the y direction. We introduce a parameter

$$\delta = \frac{\gamma_y}{\Lambda},$$

and we scale

$$\begin{aligned} (u,v,w) &= a^*(\hat{u},\delta\hat{v},\hat{w}), \\ (e_{xx},e_{xz},e_{zz}) &= \left(\tfrac{a^*}{H^*}\right)(\hat{e}_{xx},\hat{e}_{xz},\hat{e}_{zz}), \\ (\tau_{xx},\tau_{xz},\tau_{zz},\pi) &= 2B\left(\tfrac{a^*}{H^*}\right)^{\frac{1}{n}}(\hat{\tau}_{xx},\hat{\tau}_{xz},\hat{\tau}_{zz},\hat{\pi}) \\ (x,y,z,H,s,b) &= H^*\left(\hat{x},\hat{y}/\delta,\hat{z},\hat{H},\hat{s},\hat{b}\right), \\ \left(e_{xy},e_{yz}\right) &= \delta\left(\tfrac{a^*}{H^*}\right)\left(\hat{e}_{xy},\hat{e}_{yz}\right), \\ e_{yy} &= \delta^2\left(\tfrac{a^*}{H^*}\right)\hat{e}_{yy}, \\ \left(\tau_{xy},\tau_{yz}\right) &= \delta\,2B\left(\tfrac{a^*}{H^*}\right)^{\frac{1}{n}}\left(\hat{\tau}_{xy},\hat{\tau}_{yz}\right), \\ \tau_{yy} &= \delta^2\,B\left(\tfrac{a^*}{H^*}\right)^{\frac{1}{n}}\hat{\tau}_{yy}, \\ \gamma_x &= \Lambda\hat{\gamma}_x, \\ \gamma_y &= \delta\Lambda\hat{\gamma}_y, \end{aligned} \tag{A8}$$

so that the field equations may be written

$$\begin{aligned} \frac{\partial\hat{\tau}_{xx}}{\partial\hat{x}} + \delta^2\frac{\partial\hat{\tau}_{xy}}{\partial\hat{y}} + \frac{\partial\hat{\tau}_{xz}}{\partial\hat{z}} - \frac{\partial\hat{\pi}}{\partial\hat{x}} &= \hat{\gamma}_x + O(\Lambda), \\ \frac{\partial\hat{\tau}_{xy}}{\partial\hat{x}} + \delta^2\frac{\partial\hat{\tau}_{yy}}{\partial\hat{y}} + \frac{\partial\hat{\tau}_{yz}}{\partial\hat{z}} - \frac{\partial\hat{\pi}}{\partial\hat{y}} &= \hat{\gamma}_y + O(\Lambda), \\ \frac{\partial\hat{\tau}_{xz}}{\partial\hat{x}} + \delta^2\frac{\partial\hat{\tau}_{yz}}{\partial\hat{y}} + \frac{\partial\hat{\tau}_{zz}}{\partial\hat{z}} - \frac{\partial\hat{\pi}}{\partial\hat{z}} &= 0, \end{aligned} \tag{A9}$$

$$\hat{e}_{xx}^2 + \hat{e}_{xz}^2 + \hat{e}_{zz}^2 + \delta^2\left(\hat{e}_{yz}^2 + \hat{e}_{xy}^2\right) + O\left(\delta^4\right) = \hat{e}^2,$$

with boundary conditions

$$\begin{aligned} \hat{\tau}_{xz}(1,x) = \hat{\tau}_{yz}(1,x) &= 0, \\ \hat{\pi}(1,x) + \hat{\tau}_{xx}(1,x) + \hat{\tau}_{yy}(1,x) &= 0, \\ \hat{u}(0,x) = \hat{v}(0,x) = \hat{w}(0,x) &= 0. \end{aligned} \tag{A10}$$

For the cases with uniform thickness in y, we consider that all y gradients except γ_y are zero, so the solution is exact for all δ.

[71] The invariant is calculated to fourth-order accuracy. The reason for this is that $\hat{e}_{xz}^2$, $\hat{e}_{xx}^2$ can become less than $O(\delta^2)$ near the base of the divide, and the y direction terms become more important.

[72] As expected, to $O(\delta^2)$, the x and z momentum balance equations (A9) are as for plane flow. If δ^2 is sufficiently small that we can uncouple the x and y momentum balance equations, the dynamic pressure $\hat{\pi}$ is determined by the x and z momentum balance equations,

and the gradient $\partial\hat{\pi}/\partial\hat{y}$ can be deduced from the scaling relationships. Specifically, since

$$\pi = 2B\left(\frac{a^*}{H^*}\right)^{\frac{1}{n}}\hat{\pi},$$

we can immediately write down

$$\left.\frac{\partial\hat{\pi}}{\partial\hat{y}}\right|_z = -\frac{1}{n}\frac{\partial_{\hat{y}}\hat{H}}{\hat{H}}\hat{\pi} - \frac{\partial\hat{\pi}}{\partial\hat{z}}\frac{\partial\hat{Z}}{\partial x},$$
$$\frac{\partial\hat{Z}}{\partial x} = \zeta\partial_{\hat{y}}\hat{H} + \partial_{\hat{y}}\hat{b}.$$

[73] The y momentum balance equation becomes

$$\frac{\partial\hat{\tau}_{yz}}{\partial\hat{z}} + \frac{\partial\hat{\tau}_{xy}}{\partial\hat{x}} + \frac{1}{n}\frac{\partial_{\hat{y}}\hat{H}}{\hat{H}}\hat{\pi} + \frac{\partial\hat{\pi}}{\partial\hat{z}}\frac{\partial\hat{Z}}{\partial x} = \hat{\gamma}_y.$$

[74] If we adopt a power law rheology (more complex functional forms are readily accommodated), the equations are parameterized by δ and we arrive at the equation

$$\frac{\partial\hat{\varepsilon}^m\hat{\varepsilon}_{yz}}{\partial\hat{z}} + \frac{\partial\hat{\varepsilon}^m\hat{\varepsilon}_{xy}}{\partial\hat{x}} = \hat{\gamma}_y - \frac{1}{n}\frac{\partial_{\hat{y}}\hat{H}}{\hat{H}}\hat{\pi} - \frac{\partial\hat{\pi}}{\partial\hat{z}}\frac{\partial\hat{Z}}{\partial x},$$

where

$$\hat{\varepsilon}_{xy} = \frac{1}{2}\frac{\partial\hat{v}}{\partial\hat{x}}, \hat{\varepsilon}_{yz} = \frac{1}{2}\frac{\partial\hat{v}}{\partial\hat{z}},$$

or

$$\frac{\partial}{\partial\hat{z}}\left(\hat{\varepsilon}^m\frac{\partial\hat{v}}{\partial\hat{z}}\right) + \frac{\partial}{\partial\hat{x}}\left(\hat{\varepsilon}^m\frac{\partial\hat{v}}{\partial\hat{x}}\right) = 2\left(\hat{\gamma}_y - \frac{1}{n}\frac{\partial_{\hat{y}}\hat{H}}{\hat{H}}\hat{\pi} - \frac{\partial\hat{\pi}}{\partial\hat{z}}\frac{\partial\hat{Z}}{\partial x}\right), \tag{A11}$$

i.e., a nonlinear Poisson equation in $\hat{v}$. This has to be solved with the x momentum balance equation, as $\hat{\varepsilon}$ contains $\hat{\varepsilon}_{xy}$ and $\hat{\varepsilon}_{yz}$ terms. The kinematic surface condition remains the same as in the two-dimensional case.

Appendix B: Numerical Solution Technique

[75] We follow the numerical technique described by *Martín et al.* [2006]. In this section we will focus on the main improvements to that model: transient evolution of the temperature in ice and basal sliding. The model is solved iteratively by means of a procedure which uncouples the dynamical, thermal and free surface evolution submodels. The dynamic and thermal equations are solved using finite element methods, while semi-Lagrangian methods are used to solve the free surface evolution and age equations.

[76] The heat equations (6)–(8) are solved using a finite element two-point recurrence scheme [e.g., *Zienkiewicz*, 1985, Chapter 21]: the time derivative is discretized using Crank-Nicolson formula and the spatial derivatives by a Galerkin finite element method. In order to consider the thermal inertia of the bedrock a thick layer of bedrock has been included within the model domain. The deformation of the rock layer has been neglected and the thermal conductivities of rock and ice are assumed to be equal [e.g., *Pettit et al.*, 2003].

[77] A Weertman relation is considered for the basal sliding [*Weertman*, 1957]. Equation (4) can be written as

$$\tau_t{}^{(b)} = C^{-\frac{1}{m}}\left|u_t{}^{(b)}\right|^{\frac{1}{m}-1}u_t{}^{(b)}, \qquad z = b(\mathbf{r}, t), \tag{B1}$$

where $u_t^{(b)}$ and $\tau_t^{(b)}$ are the velocity and traction tangential to the bedrock surface. In the finite element model, the stress boundary condition (4) is written in terms of the basal velocities using (B1) and coupled to the finite element system [*Hindmarsh*, 1985]. Equation (B1) is then solved iteratively using the same fixed point iteration as for the ice viscosity. Weak forms of the sliding law are given by *Hindmarsh* [1985, equations (4.15)].

Notation

A	Glen's law softness parameter.
$B = (1/2)(A)^{-1/n}$	Glen's law stiffness parameter.
C	Bed slipperiness.
C_{BAED}	Relative maximum bump amplitude.
D	Ice internal dissipation.
H_d	Ice thickness at the divide.
K	Thermal conductivity.
Q	Volume flux.
Q_G	Geothermal heat flux.
Q_s	Fraction of horizontal flux due to sliding.
a	Accumulation rate of ice.
$b(\mathbf{r}, t)$	Ice bed.
$b_r(\mathbf{r}, t)$	Bottom or the rock layer.
c	Specific heat capacity.
$\mathbf{e}$	Strain rate.
m	Sliding index.
n	Glen's law index.
$s(\mathbf{r}, t)$	Ice surface.
$\mathbf{u} = (u_x, u_y)$	Horizontal velocity.
$\mathbf{v} = (u_x, u_y, w)$	Velocity vector.
v_d	Rate of divide migration.
x_d	Ice divide position.
x_d^f	Target ice divide position.
Δt_d	Time interval between two x_d^f.
Λ	Magnitude of γ_x.
Ψ	Ice age.
γ_x	Slope of the surface in the x direction at a distance H_d from the divide.
γ_y	Slope of the surface in the y direction at the divide.
$\gamma_{y(1/2)}$	Along-flow slope that halves the bump amplitude.
δ	Slope ratio.
$\delta_{(1/2)}$	Slope ratio corresponding to $\gamma_{y(1/2)}$.
θ	Temperature.
θ^f	Pressure melting point.
θ^s	Surface temperature.
κ	Thermal diffusivity of ice.
π	Dynamic pressure.
ρ	Density of ice.
$\boldsymbol{\sigma}$	Stress tensor.

$\boldsymbol{\tau}$ Deviatoric stress.
$\boldsymbol{\tau}_t$ Tangential traction.
χ Thinning rate.

[78] **Acknowledgments.** This work was funded by the U.K. Natural Environment Research Council and the Spanish National Plan for R and D (project CGL2005-05483). We are grateful to the Editor Michael Church, to the Scientific Editor Tavi Murray, to Gwendolyn J.-MC Leysinger Vieli, and to two anonymous reviewers for their helpful comments and positive discussion.

References

Blatter, H. (1995), Velocity and stress fields in grounded glaciers: A simple algorithm for including deviatoric stress gradients, *J. Glaciol.*, *41*(138), 333–344.

Boulton, G. S., and R. C. A. Hindmarsh (1987), Sediment deformation beneath glaciers: Rheology and geological consequences, *J. Geophys. Res.*, *92*, 9059–9082.

Conway, H., B. L. Hall, G. H. Denton, A. M. Gades, and E. D. Waddington (1999), Past and future grounding-line retreat of the West Antarctic Ice Sheet, *Science*, *286*, 280–283.

Dahl-Jensen, D. (1989), Steady thermomechanical flow along two-dimensional flow lines in large grounded ice sheets, *J. Geophys. Res.*, *94*(B8), 10,355–10,362, doi:10.1029/JB094iB08p10355.

Glen, J. W. (1955), The creep of polycrystaline ice, *Proc. R. Soc., Ser. A*, *228*(1175), 519–535.

Hindmarsh, R. C. A. (1985), Modelling the development of glacial erosional landforms, Ph.D. thesis, Univ. of Durham, Durham, U. K.

Hindmarsh, R. C. A. (1996), Stochastic perturbation of divide position, *Ann. Glaciol.*, *23*, 93–104.

Hindmarsh, R. C. A. (2004), A numerical comparison of approximations to the Stokes equations used in ice sheet and glacier modeling, *J. Geophys. Res.*, *109*, F01012, doi:10.1029/2003JF000065.

Hooke, R. L., B. Hanson, N. R. Iverson, P. Jansson, and U. H. Fischer (1997), Rheology of till beneath Storglaciären, Sweden, *J. Glaciol.*, *43*(143), 172–179.

Hutter, K. (1983), *Theoretical Glaciology*, D. Reidel, Dordrecht, Netherlands.

Hvidberg, C. S. (1996), Steady-state thermomechanical modelling of ice flow near the centre of large ice sheets with the finite-element technique, *Ann. Glaciol.*, *23*, 116–123.

Jacobson, H. P., and E. D. Waddington (2005), Recumbent folding of divide arches in response to unsteady ice-divide migration, *J. Glaciol.*, *51*(173), 201–209.

Kamb, B. (1991), Rheological nonlinearity and flow instability in the deforming bed mechanism of ice stream motion, *J. Geophys. Res.*, *96*(B10), 16,585–16,595, doi:10.1029/91JB00946.

Leysinger Vieli, G. J.-M. C., R. C. A. Hindmarsh, and M. J. Siegert (2007), Three-dimensional flow influences on radar layer stratigraphy, *Ann. Glaciol.*, *46*, 22–28.

Martín, C., R. C. A. Hindmarsh, and F. J. Navarro (2006), Dating ice flow change near the flow divide at Roosevelt Island, Antarctica, by using a thermomechanical model to predict radar stratigraphy, *J. Geophys. Res.*, *111*, F01011, doi:10.1029/2005JF000326.

Nereson, N. A., and C. F. Raymond (2000), The accumulation pattern across Siple Dome, West Antarctica, inferred from radar-detected internal layers, *J. Glaciol.*, *46*(152), 75–87.

Nereson, N. A., and C. F. Raymond (2001), The elevation history of ice streams and the spatial accumulation pattern along the Siple Coast West Antarctica inferred from ground-based radar data from three inter-ice-stream ridges, *J. Glaciol.*, *47*(157), 303–313.

Nereson, N. A., and E. D. Waddington (2002), Isochrones and isotherms beneath migrating ice divides, *J. Glaciol*, *48*(160), 95–108.

Nereson, N. A., R. C. A. Hindmarsh, and C. F. Raymond (1998a), Sensitivity of the divide position at Siple Dome, West Antarctica, to boundary forcing, *Ann. Glaciol.*, *27*, 207–214.

Nereson, N. A., C. F. Raymond, E. D. Waddington, and R. W. Jacobel (1998b), Migration of the Siple Dome ice divide, West Antarctica, *J. Glaciol.*, *44*(148), 643–652.

Parrenin, F., and R. C. A. Hindmarsh (2007), Influence of a non-uniform velocity field on isochrone geometry along a steady flowline of an ice sheet, *J. Glaciol.*, *53*(183), 612–622.

Pattyn, F. (2003), A new three-dimensional higher-order thermomechanical ice sheet model: Basic sensitivity, ice stream development, and ice flow across subglacial lakes, *J. Geophys. Res.*, *108*(B8), 2382, doi:10.1029/2002JB002329.

Pettit, E. C., and E. D. Waddington (2003), Ice flow at low deviatoric stress, *J. Glaciol.*, *49*(166), 359–369.

Pettit, E. C., H. P. Jacobson, and E. D. Waddington (2003), Effect of basal sliding on isochrones and flow near an ice divide, *Ann. Glaciol.*, *37*, 370–376.

Pettit, E. C., T. Thorsteinsson, H. P. Jacobson, and E. D. Waddington (2007), The role of crystal fabric in flow near an ice divide, *J. Glaciol.*, *53*(181), 277–288.

Raymond, C. F. (1983), Deformation in the vicinity of ice divides, *J. Glaciol.*, *29*(103), 357–373.

Saito, F., A. Abe Ouchi, and H. Blatter (2003), Effects of first-order stress gradients in an ice sheet evaluated by a three-dimensional thermomechanical coupled model, *Ann. Glaciol.*, *37*, 166–172.

Schoof, C. (2007), Ice sheet grounding line dynamics: steady states, stability and hysteresis, *J. Geophys. Res.*, *112*, F03S28, doi:10.1029/2006JF000664.

Tulaczyk, S., W. B. Kamb, and H. F. Engelhardt (2000), Basal mechanics of Ice Stream B, West Antarctica: 1. Till mechanics, *J. Geophys. Res.*, *105*(B1), 463–482.

Waddington, E. D., H. Conway, E. J. Steig, R. B. Alley, E. J. Brook, K. C. Taylor, and J. W. C. White (2005), Decoding the dipstick: thickness of Siple Dome, West Antarctica, at the Last Glacial Maximum, *Geology*, *33*(4), 281–284.

Weertman, J. (1957), On sliding of glaciers, *J. Glaciol.*, *3*(21), 33–38.

Wilchinsky, A. V., and V. A. Chugunov (1997), Modelling ice-divide dynamics by perturbation methods, *J. Glaciol.*, *43*(144), 352–358.

Zienkiewicz, O. C. (1985), *The Finite Element Method*, 3rd ed., McGraw-Hill, London.

R. C. A. Hindmarsh and C. Martín, Physical Sciences Division, British Antarctic Survey, Natural Environment Research Council, High Cross, Madingley Road, Cambridge CB3 0ET, UK. (rcah@bas.ac.uk; cama@bas.ac.uk)

F. J. Navarro, Departamento de Matemática Aplicada, Universidad Politécnica de Madrid, ETSI de Telecomunicación, Avenida Complutense 30, E-28040, Madrid, Spain. (fnv@mat.upm.es)